Formations of loose clusters in an unbound region of ^{12}Be

Makoto Ito

Department of Pure and Applied Physics, Kansai University, Yamatecho 3-3-35, Suita, Japan,
Research Center for Nuclear Physics (RCNP), Osaka University, Mihogaoka 10-1, Suita 567-0047, Japan, and RIKEN Nishina Center for Accelerator-based Science, RIKEN, Wako, Saitama 351-0198, Japan

(Received 16 September 2011; revised manuscript received 24 February 2012; published 10 April 2012)

The generalized two-center cluster model (GTCM), which can treat covalent and atomic configurations in general two-center systems, is applied to the light neutron-excess system $^{12}\mathrm{Be} = \alpha + \alpha + 4N$. The changes of the orbits of the neutrons are analyzed by calculating adiabatic energy surfaces with a variation of the α-α distance. The smooth transition from covalent molecular orbits to atomic He-dimer states is realized in the adiabatic energy surfaces. According to this smooth transition, the adiabatic states are divided into two regions, the internal covalent region and the external He-dimer region, by introducing boundaries of the change in structure. The intrinsic structure of the excited energy levels is investigated. We found that, in an unbound region, the He dimers appear as the molecular resonances of $\alpha + {}^{8}\mathrm{He}_{g.s.}$, ${}^{6}\mathrm{He}_{g.s.} + {}^{6}\mathrm{He}_{g.s.}$, and ${}^{5}\mathrm{He}_{g.s.} + {}^{7}\mathrm{He}_{g.s.}$. An exotic superdeformation, which has a hybrid configuration of both the covalent and He-dimer structures, is also realized in the same energy region. These unbound states can be classified into internal and external states, and the excitation degrees of freedom are assigned for the individual states. The level scheme of these unbound states reveals a strong degenerate feature with a considerable mixture of the different configurations. From the result of the level scheme, the "loose clusters" are introduced to characterize the unbound states in the neutron-excess system ^{12}Be.

DOI: 10.1103/PhysRevC.85.044308 PACS number(s): 21.60.Gx, 24.10.Eq, 25.60.Je

I. INTRODUCTION

The ground states of nuclear systems are well understood by a shell-model picture, which assumes that nucleons move in individual orbits in an average field produced by the other nucleons. In contrast, a cluster structure, in which a nucleus is decomposed into subunits, is one of the characteristic features appearing in the excited states of light nuclear systems [1]. In particular, the most famous subunit is the α particle, and typical examples are the 3α structure in 0_2^+ of ^{12}C at $E_x = 7.65$ MeV, called the Hoyle state [2,3], $\alpha + {}^{12}\mathrm{C}$ in 0_2^+ of ^{16}O at $E_x = 6.60$ MeV [4], and $\alpha + {}^{16}\mathrm{O}$ in 0_4^+ of ^{20}Ne at $E_x = 8.03$ MeV [5]. The α particle is quite inert because of a large nucleon's separation energy of $\sim$20 MeV; hence, it is considered to be a building block for light $N = Z$ systems. The multi-α structures are still current issues, and some recent studies are shown in Refs. [6,7].

The cluster structures are considered to appear according to the threshold rule [8]. The threshold rule for the $4N$ nuclei is summarized as an Ikeda diagram, which has proved to be very powerful in identifying $4N$ cluster structures (α,^{12}C,^{16}O, etc). The diagram illustrates various cluster structures that could exist in excited states of light nuclei based on the hypothesis that particular cluster structures will emerge for excitation energies near the corresponding threshold energy decaying into the respective cluster configuration. Since there are several combinations of subunits in a nucleus, cluster structures can change from level to level, and they coexist in the same nucleus with energy intervals of possible cluster decay thresholds [9,10].

Cluster degrees of freedom are also quite important in neutron-excess systems. In neutron-excess nuclei, the cluster cores are surrounded by the excess neutrons. Therefore, it is natural to introduce a model focusing on the coupling between the relative motion of the clusters and the valence neutrons. In particular, the molecular orbit (MO) model, originally proposed for $N = Z$ systems [11], is successful in describing the low-lying states of light neutron-excess nuclei [12–16]. In this model, valence neutrons perform single-particle motions in a mean field generated by cluster cores, and are similar to covalent electrons forming chemical bonds in atomic molecules. The MO model has been applied mainly to Be [12,13,17] and B [14,17] isotopes built on a structure of $\alpha + \alpha$ in ^{8}Be plus valence nucleons (N). Recent studies have extended the MO picture to other systems, such as the C isotopes ($3\alpha + N + N \cdots$) [15,18] and the Ne isotopes ($\alpha + {}^{16}\mathrm{O} + N + N \cdots$) [19,20].

The possibility exists that various cluster structures beyond the MO structure appear in the excited states, although the covalent MO model is quite successful in describing the low-lying states of the neutron-excess system. This is because, in systems with a considerable neutron excess ($N \gg Z$), there are many combinations of subunits obtained by rearrangements of excess neutrons around the cluster cores. Furthermore, their energy difference becomes small because the separation energies of the neutrons are small. Therefore, various cluster thresholds reveal a degenerate-like behavior, and this feature is in marked contrast to the case of $N = Z$ systems, where there is a large energy gap among the decay thresholds of the clusters [9,10]. From these conditions, we can generally expect that, in neutron drip-line systems, various cluster structures coexist within small energy intervals. It is an interesting subject to investigate the coexistence phenomena of various clusters of neutron-excess systems in connection to threshold rules and the low-lying MO states.

Be isotopes are typically good systems for such research subjects. Amongst them, the ^{12}Be nucleus is a very interesting

system. In its low-lying states, the breaking of the $N = 8$ magic number, which has a close connection to the MO formation, has been reported already [21,22]. In addition, the decay into $\alpha + {}^{8}\mathrm{He}_{g.s.}$ opens at 9.0 MeV, and other thresholds for decays into subunits of He isotopes appear with a small energy interval of about 1–2 MeV: 10.1 MeV for ${}^{6}\mathrm{He}_{g.s.} + {}^{6}\mathrm{He}_{g.s.}$, 11.9 MeV for ${}^{6}\mathrm{He}_{g.s.} + {}^{6}\mathrm{He}(2_1^+)$, and 13.2 MeV for ${}^{5}\mathrm{He}_{g.s.} + {}^{7}\mathrm{He}_{g.s.}$. In view of this information, various clusters with nuclear dimers of He isotopes, such as ${}^{x}\mathrm{He} + {}^{y}\mathrm{He}$, are expected to appear with a degenerate-like behavior. In fact, above the α-decay threshold, many resonant states with small energy spacings of less than 1 MeV, which strongly decay into ${}^{6}\mathrm{He}_{g.s.} + {}^{6}\mathrm{He}_{g.s.}$ and $\alpha + {}^{8}\mathrm{He}_{g.s.}$, are observed [23–27].

The MO basis are optimal configurations at the small α-α distance and are valid for describing the spatially compact states. Thus, the MO states should be classified into "internal states," which are confined in the region of the compact α-α distance. Recently, we have studied the nuclear structure of the low-lying states in ${}^{12}\mathrm{Be}$ [28] and the enhancement of monopole transitions from the ground state [29]. According to the results in Refs. [28,29], the low-lying yrast states can be nicely understood by the internal MO states [28,29]. In contrast, in the excited states, the α-α distance must be extended because of its orthogonality to the internal MO states. This spatial extension leads to the formation of the "external states" with the He dimers [30,31], which correspond to asymptotic binary channels. Therefore, nuclear structures can be divided into two parts: the internal MO and the external He-dimer states. In the present study, we analyze the structure changes from the viewpoint of the transition between the internal MO states and the external He-dimer states.

External He-dimer states are realized as the weakly bound or scattering states according to predictions of the threshold rule. This means that a scattering boundary condition is essential in order to discuss the changes from the internal MO to the external He dimer. Recently, we have developed a generalized two-center cluster model (GTCM), which can handle both the covalent MO formation and its smooth separation into binary clusters, such as the He-dimer states, in the asymptotic region [28,32]. In GTCM, basis functions for a total system are given by atomic orbital (AO) configurations with a classification of excess nucleon partitions such as $(C_1 + N_1 + N_1 + \cdots) + (C_2 + N_2 + N_2 + \cdots)$, where N_i denotes the valence nucleons localized at the ith cluster core C_i $(i = 1, 2)$. The AO basis is analogous to ionic configurations in diatomic systems, where electrons are captured by one nuclei. If we superpose various AO bases as much as possible in a variational calculation, both the MO states and the He-dimer states can be described consistently [33]. This consistent description means that it is possible to treat reaction processes such as in the formation of MOs and the decay into He dimers.

In a series of our recent studies, we have applied the GTCM to ${}^{10,12}\mathrm{Be}$ [28,29,32–36] and performed unified studies of nuclear structures and reactions. In the study of ${}^{12}\mathrm{Be}$ [28,29,34–36], global features in structural changes from MO states in a bound region to He dimers analogous to the molecular resonances (MRs) in a continuum are predicted [34]. In subsequent studies, a reaction mechanism on the formations and decay scheme of MRs through the transfer of the two neutrons, $\alpha + {}^{8}\mathrm{He}_{g.s.} \rightarrow {}^{6}\mathrm{He}_{g.s.} + {}^{6}\mathrm{He}_{g.s.}$, is investigated [35,36]. In the present paper, we report the structural transition in ${}^{12}\mathrm{Be}$ from the internal MO states to the external He-dimer states on which the scattering boundary condition is explicitly imposed. In particular, we focus on the level scheme of the resonant states above the α threshold and its intrinsic structures, in which the external states are predominant. We demonstrate that there is a degenerate-like feature in the resonant levels and all the energy levels can be characterized in terms of the internal and external states.

The organization of the present article is the following: In Sec. II, we give a detailed explanation of GTCM in connection to the two-center shell-model treatment. In Sec. III, the smooth transitions from the covalent MOs to the ionic He dimers in the adiabatic energy surfaces are shown. From the smooth transition, we introduce the "conjunction distances," which are the boundaries dividing the adiabatic states into the internal MO region and the external He-dimer region. In Sec. IV, the coupled-channels equation with the scattering boundary condition is explicitly solved on the basis of the internal MOs and the external He dimers. The obtained results of the energy spectra and their intrinsic structures are discussed. All levels are classified in terms of the squared amplitudes of the internal and external states. According to this classification, individual levels are characterized by the excitation degrees of freedom. Section V is devoted to a summary, and an anomalous feature observed in ${}^{12}\mathrm{Be}$ is characterized in terms of the "loose clusters."

II. FRAMEWORK

The brief explanations of GTCM are given in Refs. [29,32,34]. Here, we formulate GTCM from the viewpoint of the extension of the two-center shell models. The single-particle orbits for valence neutrons are constructed by the linear combination of the atomic orbitals (LCAO), in which the left-side atomic orbit $\tilde{\varphi}(L)$ and the right-side orbit $\tilde{\varphi}(R)$ are superposed as $\tilde{\varphi}(L) \pm \tilde{\varphi}(R)$.

If the atomic orbits (AOs) around individual α cores are restricted to the $0p$ wave, then there are three pairs of the covalent orbits around two α cores constructed by the LCAO treatment, and the schematic picture of the LCAO single-particle levels is shown in Fig. 1. The explicit expressions of the LCAO covalent orbits are given by

$$\pi^{\pm}_{K=+3/2} = \tilde{\varphi}(L, +1, \uparrow) \mp \tilde{\varphi}(R, +1, \uparrow), \tag{1}$$

$$\sigma^{\mp}_{K=+1/2} = \tilde{\varphi}(L, 0, \uparrow) \pm \tilde{\varphi}(R, 0, \uparrow), \tag{2}$$

$$\pi^{\pm}_{K=+1/2} = \tilde{\varphi}(L, +1, \downarrow) \mp \tilde{\varphi}(R, +1, \downarrow), \tag{3}$$

where $\tilde{\varphi}(A, l_z, \tau)$ is the $0p$-wave AO localized around one of the α clusters, which is labeled by the center A $(=L$ or $R)$, the orbital direction of l_z $(=\pm 1, 0)$, and the nucleon's spin τ $(=\uparrow$ or $\downarrow)$. All covalent orbits include the distance parameter of two α cores, S. The explicit functional form of $\tilde{\varphi}$ is taken to be the $0p$ wave function in the harmonic oscillator (HO) potential placed at each center [28]. Here, the relative coordinate between α cores is taken to be the z axis for the

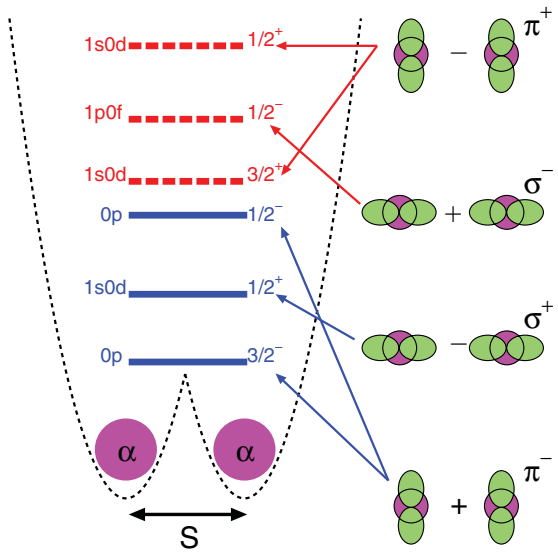

FIG. 1. (Color online) Schematic picture of the single-particle levels around two α cores. The solid and dashed lines represent the binding and antibinding orbitals, respectively. The naive shell-model orbit, corresponding to MO in the zero limit of the α-α distance ($\mathbf{S} \to 0$), is shown in the left part of the single-particle energy levels. The half integers at the right part represent the K^π quantum number.

definition of the K-quantum number, and all of the orbits have good K-quantum numbers. The extension of AO to the higher shell-model orbits, such as $1s, 0d, 1p, \ldots$, can also be done in a straightforward manner, although in the present studies AOs are restricted to the lowest unoccupied orbit, $0p$, for simplicity.

In Eqs. (1)–(3), the orbits with a lower sign are called the "binding orbits," while those with an upper sign are called the "antibinding orbits." In general, energies of the binding orbits are lower than those of the antibinding orbits because the latter orbits have an additional node along the α-α axis in comparison with the former orbits. In Fig. 1, the location of the single-particle level is shown schematically by the solid and dashed levels for the binding and antibinding orbits, respectively. At the left part of the single-particle levels, we show the naive shell-model orbits, to which the covalent orbits correspond in the zero limit of the α-α distance. As can be confirmed from Fig. 1, we consider the covalent orbits around two α cores up to the $1p0f$ configuration for the excess neutrons in the present treatment, in which AO is restricted to the $0p$ shell.

When four excess neutrons occupy these three pairs of the covalent orbits, various MO configurations can be obtained, such as $(\pi^-_{3/2})^2(\sigma^+_{1/2})^2$, $(\pi^-_{3/2})^2(\pi^-_{1/2})^2$, and so on. According to the LCAO approximation, general MO configurations, which are the product of the orbits in Eqs. (1)–(3), are constructed by the linear combination of the AO wave function of four neutrons,

$$\prod_{j=1}^{4} \tilde{\varphi}_j(A_j, l_{zj}, \tau_j), \tag{4}$$

where A, l_z, and τ have a subscript of the neutron number j. Furthermore, each of the $0p$-wave AOs, $\tilde{\varphi}(A, l_z, \tau)$, having a good K-quantum number, can be expressed by the orbits defined in Cartesian coordinates such as

$$\tilde{\varphi}(A, \pm 1, \tau) = \mp\varphi(A, x, \tau) - i\varphi(A, y, \tau), \tag{5}$$

$$\tilde{\varphi}(A, 0, \tau) = \varphi(A, z, \tau). \tag{6}$$

Here, $\varphi(A, k, \tau)$ with $k = x, y, z$ denotes a similar $0p$-wave AO to $\tilde{\varphi}(A, l_z, \tau)$, but it is a function in Cartesian coordinates. Because of the equivalence in Eqs. (5) and (6), we can employ the direct products of φ in Cartesians coordinate as basis functions in describing the general MO motions of the four neutrons, instead of the products of the orbits of $\tilde{\varphi}$ with spherical harmonics.

The basis function $\{\Phi^{J^\pi}_{\mathbf{m}}(S)\}$, which contains the α cores' degree of freedom explicitly, is given by

$$\Phi^{J^\pi}_{\mathbf{m}}(S) = \hat{P}^{J^\pi}_{K=0}\, \mathcal{A}\left\{\psi_L(\alpha)\psi_R(\alpha)\prod_{j=1}^{4}\varphi_j(m_j)\right\}_S. \tag{7}$$

The α cluster $\psi_n(\alpha)$ $(n = L, R)$ is expressed by the $(0s)^4$ configuration of the HO potential centered at the left (L) or right (R) side with the relative distance S [37]. $\varphi_j(m_j)$ represents the $0p$-wave AO for the jth neutrons in Cartesian coordinates, and $\{m_j\}$ are indices of AO (A, k, τ). In the left-hand side of Eq. (7), $\mathbf{m}$ represents a set of AOs for the four neutrons, $\mathbf{m} = (m_1, m_2, m_3, m_4)$. The intrinsic basis functions with the full antisymmetrization $\mathcal{A}$ are projected to the eigenstate of the total spin parity J^π and its intrinsic angular projection K, which is restricted to the axial symmetric case $(K = 0)$ by the projection operator $\hat{P}^{J^\pi}_K$. The restriction to the axial symmetric configurations for the low-energy phenomena has already been justified in studies of the sub-barrier fusion reaction based on the time-dependent wave-packet approach [38].

The wave function of ^{12}Be is finally given by taking a superposition over the relative distance parameter S and $\mathbf{m}$ as

$$\Psi^{J^\pi}_\nu = \int dS \sum_{\mathbf{m}} C^{J^\pi\nu}_{\mathbf{m}}(S)\, \Phi^{J^\pi}_{\mathbf{m}}(S). \tag{8}$$

It should be stressed that the total wave function in Eq. (8) with the basis in Eq. (7) can reproduce not only MO configurations but also the asymptotic binary channels composed of the He dimers, such as $\alpha + {}^8$He $[A_1A_2A_3A_4 = LLLL$ or $RRRR$ in Eq. (7)], ^{6}He + ^{6}He ($LLRR$ or $RRLL$), and ^{5}He + ^{7}He ($LLLR$ or $RRRL$). The detailed explanation of the flexibility and advantages of our wave function is given in Ref. [29].

The coefficients $C^{J^\pi\nu}_{\mathbf{m}}(S)$ in Eq. (8) for the νth eigenstate are determined by solving a coupled-channel generator coordinate method) (GCM) equation [37],

$$\left\langle \Phi^{J^\pi}_{\mathbf{m}}(S)\middle| H - E^{J^\pi}_\nu \middle|\Psi^{J^\pi}_\nu\right\rangle = 0. \tag{9}$$

The bound states below the particle decay threshold are calculated by a diagonalization procedure, while the scattering boundary condition is explicitly imposed above the threshold. The details of the scattering boundary condition will be explained in the later sections.

As for the NN interaction, we use the Volkov No.2 and G3RS for the central and spin-orbit parts, respectively. The details of the parameters in the interactions and the size

TABLE I. Comparisons of the threshold energies in the calculation with those in the experiment. The energy is shown in units of MeV. The parameters of Volkov No.2 are $M = 0.643$ and $B = H = 0.125$, while the strength of G3RS is taken to be +3000 MeV and −2000 MeV for the repulsive and attractive parts, respectively. The radius parameter of harmonic oscillator b is fixed to 1.46 fm.

Channel	Experiment	Calculation
$\alpha + {}^8\mathrm{He}_{g.s.}$	9.0	9.3
${}^6\mathrm{He}_{g.s.} + {}^6\mathrm{He}_{g.s.}$	10.1	11.8
${}^6\mathrm{He}_{g.s.} + {}^6\mathrm{He}(2_1^+)$	11.9	13.7
${}^5\mathrm{He}_{g.s.} + {}^7\mathrm{He}_{g.s.}$	13.2	14.6

parameter of HO are explained in Ref. [28]. In Table I, the calculated thresholds for the lowest four open channels are shown. The energy difference of $\alpha + {}^8\mathrm{He}_{g.s.}$ and ${}^6\mathrm{He}_{g.s.} + {}^6\mathrm{He}_{g.s.}$ in the calculation is a little larger than that in the experiments, but the relative differences among the thresholds are reasonably reproduced by the present NN interaction. Since the threshold energy corresponds to the order of magnitude of the interaction strength to dissociate a compound system into a pair of clusters, the reproduction of the threshold energy is crucial in discussing the formation of cluster structures.

III. ADIABATIC ENERGY SURFACES

A. Transition from internal states to external states in AESs

Before solving the full equation with $J^\pi = 0^+$, we solve Eq. (9) at a fixed S,

$$\langle \Phi_{\mathbf{m}}(S)|H - E_\mu(S)\big|\Phi^\mu_{AS}(S)\big\rangle = 0, \tag{10}$$

$$\Phi^\mu_{AS}(S) = \sum_{\mathbf{m}'} D^\mu_{\mathbf{m}'}(S)\Phi_{\mathbf{m}'}(S). \tag{11}$$

The eigenvalue $E_\mu(S)$ and the mixing amplitude $D^\mu_{\mathbf{m}}(S)$ for the μth state depend on the relative distance parameter S. We call the solutions of energies $E_\mu(S)$ and wave functions $\Phi^\mu_{AS}(S)$ "adiabatic energy surfaces" (AESs) and "adiabatic states" (ASs), respectively. In Eqs. (10) and (11), the quantum number of $J^\pi = 0^+$ is omitted for simplicity. The calculated AESs for the $J^\pi = 0^+$ state are shown in Fig. 2. In the present calculation, we obtained 38 AESs, and the lowest four AESs are plotted in this figure.

Below the $\alpha + {}^8\mathrm{He}_{g.s.}$ threshold, two local minima appear at $S \sim 3.6$ fm in the dashed (A) and solid (B) curves. A detailed analysis on the coupling scheme of the lowest two AESs has been done in Refs. [28,29]. Around these minima, each valence neutron rotates around both α clusters, and the MO structure is formed. In contrast, in the energy region above the threshold, two AESs (C) and (D) with shallow minima appear. Around the shallow minima, exotic structures different from the simple MO structure are realized. In the following subsection, we show a detailed analysis of the changes in structure in the AESs.

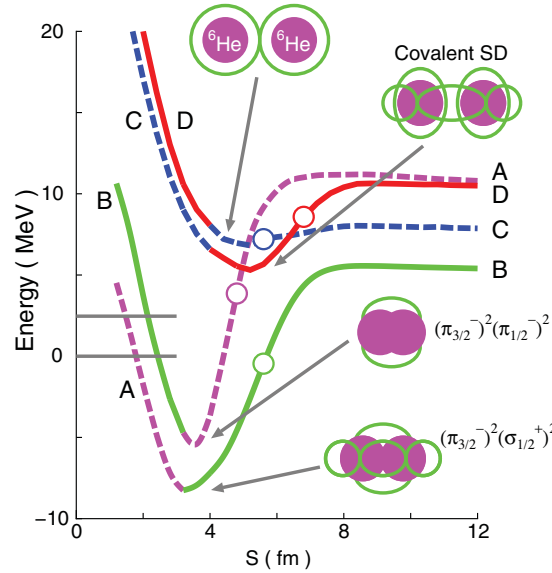

FIG. 2. (Color online) Adiabatic energy surfaces (AESs) for $J^\pi = 0^+$. The calculated thresholds for the open channels, $\alpha + {}^8\mathrm{He}_{g.s.}$ (origin of the ordinate) and ${}^6\mathrm{He}_{g.s.} + {}^6\mathrm{He}_{g.s.}$ are also shown. The circles on the AESs represent the boundary of the internal MO state and the external He-dimer state. See text for details.

1. AES in the bound region

The main configuration of the solid curve (B) at the minimum is $(\pi^-_{3/2})^2(\sigma^+_{1/2})^2$, while curve (A) has the dominant configuration of $(\pi^-_{3/2})^2(\pi^-_{1/2})^2$ for the four neutrons, as shown by the schematic picture in Fig. 2. The former and latter MO configurations correspond to $(0p)^2(1s0d)^2$ and $(0p)^4$ configurations at the limit of $S = 0$, respectively. The AESs show the interchange of the main components around the minimum point; hence, the strong mixing of these configurations occurs around the optimal S value. As S increases, these two surfaces are continuously changed to $\alpha + {}^8\mathrm{He}_{g.s.}$ (B) and ${}^5\mathrm{He}_{g.s.} + {}^7\mathrm{He}_{g.s.}$ (channel spin $I = 2$) (A) in the outside region of the circles.

The interchange of (A) and (B) is generated by a crossing of the unperturbed (diabatic) energy curve of $(\pi^-_{3/2})^2(\sigma^+_{1/2})^2$ and $(\pi^-_{3/2})^2(\pi^-_{1/2})^2$. The energy of the pure $(\pi^-_{3/2})^2(\sigma^+_{1/2})^2$ configuration is higher than that of $(\pi^-_{3/2})^2(\pi^-_{1/2})^2$ because the latter MO state has a large component of the closed-shell configuration of the neutrons, $\nu(0p)^6$. However, there is a large correlation energy for $(\pi^-_{3/2})^2(\sigma^+_{1/2})^2$, which arises from the coupling to the spin triplet configuration of $(\pi^-_{3/2})^2(\sigma^+_{1/2}\pi^+_{1/2})$ [28,29]. Due to this correlation energy, the diabatic energy of $(\pi^-_{3/2})^2(\sigma^+_{1/2})^2$ becomes comparable to that of $(\pi^-_{3/2})^2(\pi^-_{1/2})^2$, and the coupling between them strongly occurs as shown in Fig. 2.

2. AES in the continuum

The dashed curve (C) has a specific character such that the continuous change from MO to a He dimer occurs at a small α-α distance. In the small-S region where the two α clusters strongly overlap, this surface has a pure covalent

MO configuration of $(\pi^-_{3/2})^2(\pi^+_{3/2})^2$. Substituting Eq. (1) for $(\pi^-_{3/2})^2(\pi^+_{3/2})^2$ and considering the antisymmetrization among the four neutrons, we can get the following expression for this MO configuration:

$$\mathcal{A}\{(\pi^-_{3/2})^2(\pi^+_{3/2})^2\} = \mathcal{A}\{\tilde{\varphi}(L,+1,\uparrow)\tilde{\varphi}(L,-1\downarrow)\tilde{\varphi}(R,+1,\uparrow)\tilde{\varphi}(R,-1\downarrow)\}. \quad (12)$$

This MO configuration contains a pair of neutrons at the left and right sides. Thus, this MO configuration is identical to the ^{6}He + ^{6}He cluster state. In general MO configurations, three partitions, α + ^{8}He, ^{6}He + ^{6}He, and ^{5}He + ^{7}He, are coherently mixed with each other [28], but, in $(\pi^-_{3/2})^2(\pi^+_{3/2})^2$, only the ^{6}He + ^{6}He partition survives because of the antisymmetrization effect. Such a selection of a specific partition always occurs when the excess neutrons equally occupy both the binding $[(\pi^-_{3/2})^2]$ and antibinding $[(\pi^+_{3/2})^2]$ orbits. The main component of (C) finally changes to ^{6}He$_{g.s.}$ + ^{6}He$_{g.s.}$ in the large-S region beyond the circles.

Around the energy minimum point of the solid curve (D), two of the valence neutrons are localized around the individual α as ^{5}He + ^{5}He, which is the AO structure, and the remaining two neutrons occupy the σ^+ orbital and rotate around both clusters, which represents the MO character. Specifically, the minimum state of (D) has an intermediate character of MO and He dimers, and its configuration is constructed from Eqs. (1) and (2) as

$$\mathcal{A}\{\tilde{\varphi}(L)\,\tilde{\varphi}(R)\,(\sigma^+_{1/2})^2\} \quad (13)$$

with the definitions

$$\tilde{\varphi}(L) \equiv \tilde{\varphi}(L,+1,\uparrow) = (\pi^-_{+3/2} + \pi^+_{+3/2}),$$
$$\tilde{\varphi}(R) \equiv \tilde{\varphi}(R,-1\downarrow) = (\pi^-_{-3/2} - \pi^+_{-3/2}). \quad (14)$$

The localized orbits of $\tilde{\varphi}(L)$ and $\tilde{\varphi}(R)$ can be obtained by an equal mixing of the binding $(\pi^-_{3/2})$ and antibinding $(\pi^+_{3/2})$ covalent orbits. Because of the two neutrons in the σ orbital, the clustering (the optimal S value) is enhanced in the same way as in the second 0^+ state of ^{10}Be [13,32,33]. In this paper, we call this strongly deformed state with the covalent neutrons the covalent superdeformed (covalent SD) state. The covalent SD state finally changes to the He dimer of ^{5}He$_{g.s.}$ + ^{7}He$_{g.s.}$ ($I = 0$) outside region of the circle.

B. Adiabatic conjunction

In this section, we show a feature of the adiabatic conjunction, which is a smooth transition from the internal MO states to the external He-dimer states, and define the conjunction distance, which is the boundary between the internal states and the external states. To confirm the features of the adiabatic conjunction clearly, we show the squared overlap of the lowest ($\mu = 1$) adiabatic state (AS), $\Phi^{\mu=1}_{AS}(S)$, and the MO or He-dimer state, $\phi^{\gamma}(S)$, where γ represents a kind of MO or He-dimer configuration. The squared overlap $f^{\gamma}(S)$ is defined by

$$f^{\gamma}(S) = \left|\left\langle \phi^{\gamma}(S)\middle|\Phi^{\mu=1}_{AS}(S)\right\rangle\right|^2. \quad (15)$$

For the overlap with γ = MO states, we consider

$$(\pi^-_{3/2})^2(\pi^-_{1/2})^2, \quad (\pi^-_{3/2})^2(\sigma^+_{1/2})^2, \quad (\pi^-_{3/2})^2(\sigma^+_{1/2}\pi^+_{1/2}), \quad (16)$$

while, for the overlap with γ = He-dimer states, we prepare

$$\alpha + {}^8\mathrm{He}_{g.s.}, \quad {}^6\mathrm{He}_{g.s.} + {}^6\mathrm{He}_{g.s.}, \quad {}^5\mathrm{He}_{g.s.} + {}^7\mathrm{He}_{g.s.}\ (I=0). \quad (17)$$

The overlap with the MO states is shown in Fig. 3(a). The $\mu = 1$ adiabatic state contains various MO configurations, but $(\pi^-_{3/2})^2(\pi^-_{1/2})^2$ and $(\pi^-_{3/2})^2(\sigma^+_{1/2})^2$ in Eq. (16) are the main components. At the inner region of $S \leqslant 3.4$ fm, the amplitude of $(\pi^-_{3/2})^2(\pi^-_{1/2})^2$ is dominant, as shown by the dot-dashed curve (inverse triangles) in Fig. 3(a). However, the amplitude suddenly decreases as the distance becomes larger, and the main component is replaced by $(\pi^-_{3/2})^2(\sigma^+_{1/2})^2$ around the distance of $S \sim 3.6$ fm, which is the interchange point in Fig. 2. This sudden transition is generated by the crossing of the diabatic energy curves of these two MO configurations. The amplitude of $(\pi^-_{3/2})^2(\sigma^+_{1/2})^2$ is dominant up to $S = 5$ fm and finally decreases beyond $S = 6.4$ fm.

In the region with a dominance of $(\pi^-_{3/2})^2(\sigma^+_{1/2})^2$, there is a considerable mixture of $(\pi^-_{3/2})^2(\sigma^+_{1/2}\pi^+_{1/2})$, which has a triplet-odd configuration. As confirmed in Refs. [28,29], the coupling to the triplet-odd state gives a large binding energy gain for $(\pi^-_{3/2})^2(\sigma^+_{1/2})^2$. As a result of this coupling effect, a considerable mixture of $(\pi^-_{3/2})^2(\sigma^+_{1/2}\pi^+_{1/2})$ appears in the $\mu = 1$ adiabatic state.

The overlap with the He-dimer states is shown in Fig. 3(b). At the short distance of $S \sim 1$ fm, where two α cores strongly overlap, the squared amplitude of these three He-dimer channels reaches about unity. This means that these channels cannot be distinguished at a small S because of the antisymmetrization effect among nucleons [37]. The strong mixture of the three channels continues up to $S \sim 3$ fm, where a clear component of $(\pi^-_{3/2})^2(\pi^-_{1/2})^2$ can be observed in Fig. 3(a). At $S \sim 4$ fm, the component of ^{5}He$_{g.s.}$ + ^{7}He$_{g.s.}$ completely decreases, and the dominant amplitude of the MO configuration also changes from $(\pi^-_{3/2})^2(\pi^-_{1/2})^2$ to $(\pi^-_{3/2})^2(\sigma^+_{1/2})^2$ at the same S. With the limit of the larger S, where $(\pi^-_{3/2})^2(\sigma^+_{1/2})^2$ is suppressed, the adiabatic state changes to the pure α + ^{8}He$_{g.s.}$ cluster state.

In the arrow region ($5 \leqslant S \leqslant 6.4$ fm) shown in Figs. 3(a) and 3(b), the amplitude of α + ^{8}He$_{g.s.}$ begins to increase, while $(\pi^-_{3/2})^2(\sigma^+_{1/2})^2$ begins to decrease in the same region. Thus, the transition of $(\pi^-_{3/2})^2(\sigma^+_{1/2})^2 \to \alpha$ + ^{8}He$_{g.s.}$ can be confirmed in the arrow region. It should be noticed that this transition from MO to the dimer state gradually occurs in contrast to the sudden transition induced by the level crossing, $(\pi^-_{3/2})^2(\pi^-_{1/2})^2 \to (\pi^-_{3/2})^2(\sigma^+_{1/2})^2$. In addition, this smooth transition does not involve any avoided crossing as can be seen in Fig. 2. Such a continuous transition is defined as the adiabatic conjunction [29]. In the conjunction region of $S = 5$–6.4 fm, the main component of $(\pi^-_{3/2})^2(\sigma^+_{1/2})^2$ begins to go into the α + ^{8}He$_{g.s.}$ channel. Therefore, the adiabatic state at the conjunction region has an intermediate character of MO and an asymptotic cluster.

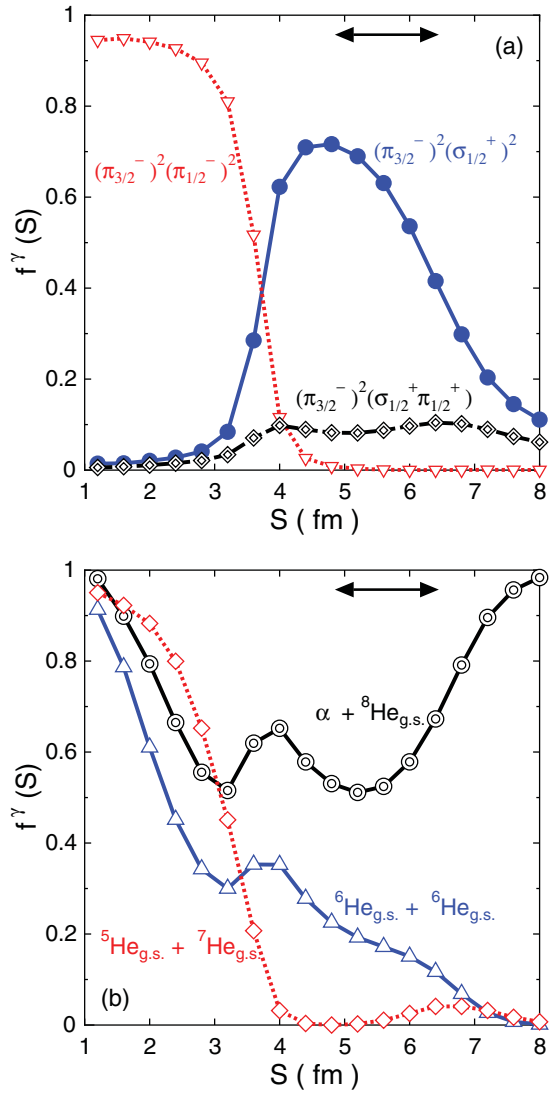

FIG. 3. (Color online) (a) Squared overlap of the lowest adiabatic states and the MO states. The inverse triangles show the squared magnitude of $(\pi_{3/2}^-)^2(\pi_{1/2}^-)^2$, while the circles and the diamonds represent that of $(\pi_{3/2}^-)^2(\sigma_{1/2}^+)^2$ and $(\pi_{3/2}^-)^2(\sigma_{1/2}^+\pi_{1/2}^+)$, respectively. (b) The same as in panel (a), except for the overlap with the cluster states. The double circles, the triangles, and the diamonds represent the cluster channels of $\alpha + {}^8\mathrm{He}_{g.s.}$, ${}^6\mathrm{He}_{g.s.} + {}^6\mathrm{He}_{g.s.}$, and ${}^5\mathrm{He}_{g.s.} + {}^7\mathrm{He}_{g.s.}$, respectively.

From the analysis of the squared overlap, we can define the "conjunction distance," S_C, at which the transition from MO to He dimer occurs. As the distance parameter S becomes larger, the amplitude of MO and the He dimer decreases and increases, respectively. Therefore, the conjunction distance is defined by the point where the squared amplitude of MO (or the He dimer) falls below (or exceeds) 50%. In the case of Fig. 3, S_C can be identified as 5.6 fm because, beyond this distance, the population of $(\pi_{3/2}^-)^2(\sigma_{1/2}^+)^2$ falls below 50%, while that of $\alpha + {}^8\mathrm{He}_{g.s.}$ exceeds 50%. In the higher-energy region, the assignment of S_C becomes difficult due to the high level density of the AESs. However, we can fix S_C by employing the criterion that either the He-dimer amplitude exceeds 50% or the MO amplitude falls below 50%.

TABLE II. Conjunction distance (S_C) and the dominant configurations of the internal ($S \leqslant S_C$) and external regions ($S \geqslant S_C$). S_C is in units of fm. See text for details.

AES	S_C	Internal ($S \leqslant S_C$)	External ($S \geqslant S_C$)
A	4.8	$(\pi_{3/2}^-)^2(\pi_{1/2}^-)^2$	${}^5\mathrm{He}_{g.s.} + {}^7\mathrm{He}_{g.s.}$ ($I = 2$)
B	5.6	$(\pi_{3/2}^-)^2(\sigma_{1/2}^+)^2$	$\alpha + {}^8\mathrm{He}_{g.s.}$
C	5.6	$(\pi_{3/2}^-)^2(\pi_{3/2}^+)^2$	${}^6\mathrm{He}_{g.s.} + {}^6\mathrm{He}_{g.s.}$
D	7.2	$[\tilde{\varphi}(L)\tilde{\varphi}(R)\,(\sigma_{1/2}^+)]^2$	${}^5\mathrm{He}_{g.s.} + {}^7\mathrm{He}_{g.s.}$ ($I = 0$)

The identified S_C is shown in Table II. The S_C is a boundary between the internal MO state and the external He-dimer state. The dominant MO ($S \leqslant S_C$) and He dimer ($S \geqslant S_C$) are shown in the same table, and the identified S_C are also plotted in Fig. 2 by the circles. S_C of (A)–(C) is close to the barrier-top position of the He-dimer state. In particular, S_C for (D) is the largest of all the AESs. This is because the pair transfer of the neutrons strongly activates over a large α-α distance because of the σ^+-orbital formation.

C. The orthogonality effect and cluster formation

In the previous section, we confirmed the smooth transition between the internal MO states and the external He-dimer states in AESs. The internal MO state appears as a local minimum state in the internal region of the α-α distance. The stable energy level is generated by the internal MO states around the local minimum when the variational equation (9), which superposes all the adiabatic states, is fully solved. However, such a local minimum, which is an ingredient for the formation of an energy level, does not exist for the external He-dimer state. In the formation of the energy levels with the He-dimer states, the orthogonality effect is essential. In this section, we discuss the formation mechanism of the external He-dimer states in connection with the orthogonality condition.

The orthogonality to the internal MO states plays an important role in the formation of the He-dimer states. To see the orthogonality effect clearly, we calculate AESs by employing the orthogonalized AO basis

$$\tilde{\Phi}_{\mathbf{m}}(S) = \Phi_{\mathbf{m}}(S) - \sum_{\nu=1,2} \Psi_\nu \langle \Psi_\nu | \Phi_{\mathbf{m}}(S) \rangle. \qquad (18)$$

In Eq. (18), Ψ_ν represents the wave function of the ground 0_1^+ ($\nu = 1$) and the first excited 0_2^+ ($\nu = 2$) states, which are obtained in the full calculation shown in Eq. (9). The 0_1^+ and 0_2^+ states are mainly generated by the superpositions of the adiabatic states around the lowest and second minima with (A) and (B) in Fig. 2 as discussed in Refs. [28,29]. Thus, in the model space spanned by Eq. (18), the components of the internal MO states, which have a spatially compact structure, are excluded. This exclusion means that we can clearly observe the He-dimer formation in the complementary space to the low-lying MO states.

The AESs calculated in the orthogonalized AO space are shown by the dotted and dot-dashed curves in Fig. 4. The dotted curve is calculated with the orthogonality condition

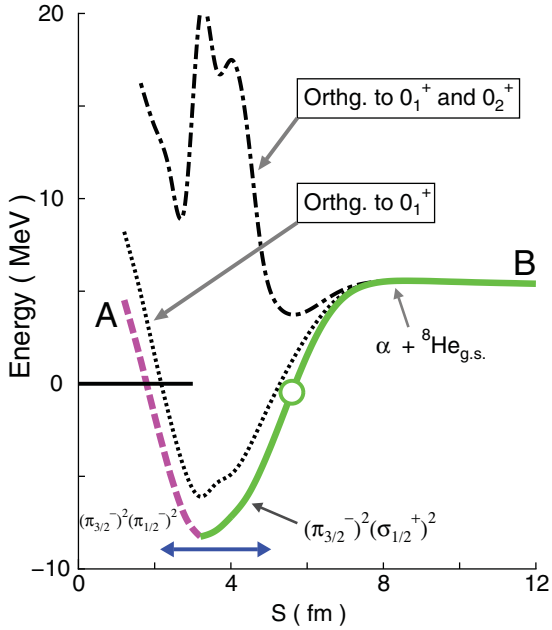

FIG. 4. (Color online) Lowest AES with the orthogonality condition. The AESs (A) and (B) are the same as those plotted in Fig. 2. The dotted and dot-dashed curves represent the results with orthogonality to the 0_1^+ and $(0_1^+ + 0_2^+)$ states, respectively. The $\alpha + {}^8\mathrm{He}_{g.s.}$ threshold is taken to be the zero energy in the ordinate. The horizontal arrow shows the dominant range of S in the 0_1^+ and 0_2^+ states. The circle represents the conjunction distance identified in Table II.

to the ground 0_1^+ state, while the orthogonality to 0_1^+ and 0_2^+ is taken into account for the dot-dashed curve. When we impose the orthogonality to 0_1^+, the resultant dotted curve is slightly shifted and still has a deep minimum, which is a similar shape to the second AES in Fig. 2. The shifted minimum corresponds to the other low-lying state, 0_2^+. The minimum of the dot-dashed curve, calculated in the complementary space to both the 0_1^+ and 0_2^+ states, is much shallower than that of the dotted curve. This shallow minimum corresponds to the 0_3^+ state, and its energy position is close to the $\alpha + {}^8\mathrm{He}_{g.s.}$ threshold (the origin of the vertical axis). The 0_3^+ state in the full calculation appears just above the respective threshold by about 1 MeV, as shown in Sec. IV. Such a cluster formation due to the orthogonality is a general phenomena, which can be observed in an excited state of light nuclei [1].

In the dot-dashed curve, there is a strong repulsive core at $S \leqslant 5$ fm, and this structure core is generated so as to avoid the internal region [39] shown by the horizontal arrow, which is a main component contained in the 0_1^+ and 0_2^+ states. Due to a strong repulsive core at the inner region, which prevents α and $^8\mathrm{He}_{g.s.}$ from merging together, the 0_3^+ state has a large component of the weakly coupled $\alpha + {}^8\mathrm{He}_{g.s.}$ structure. The minimum point of the dot-dashed curve is just the same as the conjunction distance, $S_C = 5.6$ fm (circle), where a smooth transition of the internal $(\pi_{3/2}^-)^2(\sigma_{1/2}^+)^2$ and the external $\alpha + {}^8\mathrm{He}_{g.s.}$ occurs. This means that the smooth change is important for the formation of the 0_3^+ state, which has a well-developed $\alpha + {}^8\mathrm{He}_{g.s.}$ structure.

IV. ENERGY SPECTRA OF THE $J^\pi = 0^+$ STATES

A. The scattering boundary condition

Above the particle decay threshold, the formation and decays of the internal states occur through the external state. This means the scattering boundary condition should be explicitly imposed on the external He-dimer states when the system is excited above the particle decay threshold. An external He-dimer state is completely the same as the channel wave function, which is the basis in the scattering problem. Thus, we can naturally impose the scattering boundary condition on the external states, and the coupling of the internal states and the external states can be solved. An explicit form of the channel wave function is given by

$$\chi_{\beta L}^{J^\pi}(\mathbf{R}_\beta, S) = \mathcal{A}\left\{\Gamma_L(R_\beta, S)\ \hat{\Phi}_{\beta L}^{J^\pi}(\hat{\mathbf{R}}_\beta, \xi_\beta)\right\}, \qquad (19)$$

where $\hat{\Phi}_{\beta L}^{J^\pi}(\hat{\mathbf{R}}_\beta, \xi_\beta)$ denotes the internal wave function for the channel $\beta \equiv (n_1, n_2, I_1, I_2, I)$, which is designed by a combination of the intrinsic spin of the colliding He nuclei, (I_1, I_2), the channel spin I with $\mathbf{I} = \mathbf{I}_1 + \mathbf{I}_2$, and other quantum numbers (n_1, n_2) which are needed to specify the combination of the scattering He isotopes (excitation energies and so on). $(R_\beta, \hat{\mathbf{R}}_\beta)$ represent the radial and angular part of the relative coordinate between two He nuclei in channel β, and L represents the conjugate momentum of $\hat{\mathbf{R}}_\beta$. $\Gamma_L(R, S)$ is the radial basis function, which has a local peak around the distance of $R \sim S$ [37].

The total wave function in Eq. (8) is expanded by the channel wave function in Eq. (19), and the resultant coupled-channels equations are solved under the scattering boundary condition. The scattering boundary condition can be imposed on individual channels by employing the Kohn-Hulthén-Kato variational method [33,34,40,41]. In the present calculation, the computational procedure is the same as in the method with the trial function (II) shown in Ref. [41].

In the present model space of the AO basis, we can construct the 38 channels for $J^\pi = 0^+$, which are the $\alpha + {}^8\mathrm{He}$, ${}^5\mathrm{He} + {}^7\mathrm{He}$, and ${}^6\mathrm{He} + {}^6\mathrm{He}$ partitions. The possible internal states of the He nucleus are shown in Table III. In solving the scattering problem, we include all 38 channels, which is much more channels than the previous coupled-channel calculation of $(\alpha + {}^8\mathrm{He}_{g.s.}) + ({}^6\mathrm{He}_{g.s.} + {}^6\mathrm{He}_{g.s.})$ in Ref. [30].

B. Energy levels

By imposing the appropriate boundary conditions, we obtain whole energy spectra from the bound states to the unbound states as shown in Fig. 5 ($J^\pi = 0^+$). In this figure,

TABLE III. Spin-parity states of the He isotopes included in the present calculation. Individual states are shown in order of their excitation energy.

^{5}He	$3/2^-, 1/2^-$
^{6}He	$0_1^+, 2_1^+, 2_2^+, 1^+, 0_2^+$
^{7}He	$3/2_1^-, 5/2^-, 3/2_2^-, 1/2^-, 3/2_3^-$
^{8}He	$0_1^+, 2_1^+, 2_2^+, 0_2^+$

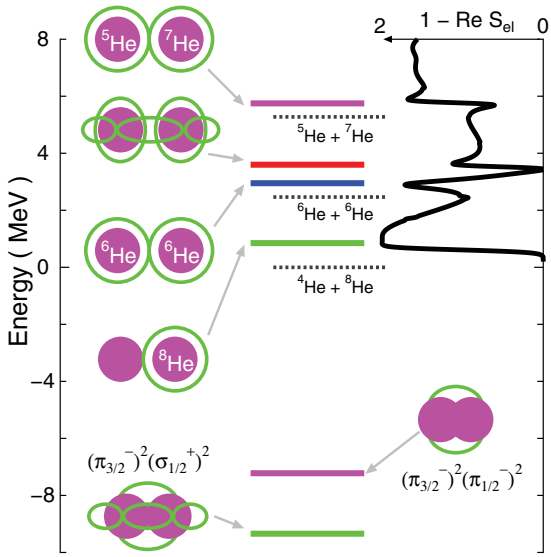

FIG. 5. (Color online) Energy spectra for $J^\pi = 0^+$. The solid curve at the right part shows the total reaction probability of the $\alpha + {}^8\mathrm{He}_{g.s.}$ scattering with a scale at the top axis. The dotted lines represent the threshold energy of the open channels considered in the calculation.

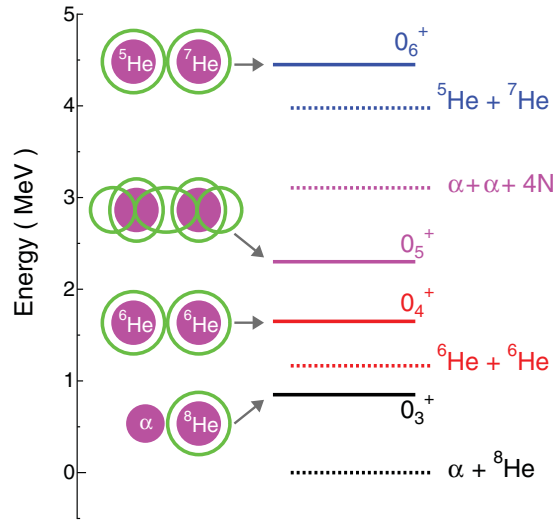

FIG. 6. (Color online) Energy levels in the continuum. The threshold for the binary He channels (calculation) and the $\alpha + \alpha + 4N$ (experiment) are shown by the dotted lines, while the energy levels are plotted by the solid lines. The threshold and the energy levels above $E = 1$ MeV are shifted by about 1.3 MeV. See text for details.

the total reaction probability, which is defined by $1 - \Re S_{el}$ with the elastic S matrix of S_{el}, is also shown.

We can clearly observe the formation of the various chemical bonding-like structures in the calculated spectra. The obtained 0^+ states are classified into three categories: (i) MO states: Two bound states, 0^+_1 and 0^+_2, appear below the $\alpha + {}^8\mathrm{He}_{g.s.}$ threshold. Here the four neutrons are in MO motion around the two α cores $[(\pi^-_{3/2})^2(\sigma^+_{1/2})^2$ in 0^+_1 and $(\pi^-_{3/2})^2(\pi^-_{1/2})^2$ in $0^+_2]$. (ii) MR states: The resonant states, 0^+_3, 0^+_4, and 0^+_6, have the He-dimer configuration of the corresponding threshold, $\alpha + {}^8\mathrm{He}_{g.s}$, ${}^6\mathrm{He}_{g.s.} + {}^6\mathrm{He}_{g.s.}$, and ${}^5\mathrm{He}_{g.s.} + {}^7\mathrm{He}_{g.s.}$, respectively. The relative wave function between two He nuclei is largely extended and, hence, these resonant states can be interpreted in terms of the molecular resonances (MRs), composed of the He dimers. (iii) Covalent SD state: The main component of 0^+_5 is the mixture of $(\sigma^+_{1/2})^2$ and ${}^5\mathrm{He} + {}^5\mathrm{He}$. Due to the $(\sigma^+_{1/2})^2$ formation, this state has a large clustering ($S \sim 5$ fm) in comparison with the radius of an α particle ($\sim$1.4 fm).

A comparison of the levels with the respective He-decay thresholds is summarized in Fig. 6. In this figure, the six-body channel, $\alpha + \alpha + 4N$, is also plotted, although the degree of freedom for the six-body decay is not considered in the present calculation. Since the calculated threshold difference, $\Delta E = E_{th}({}^6\mathrm{He}_{g.s.} + {}^6\mathrm{He}_{g.s.}) - E_{th}(\alpha + {}^8\mathrm{He}_{g.s.})$, is larger by about 1.3 MeV than the experimental value (See Table I), the thresholds and the energy levels above $E_{th}({}^6\mathrm{He}_{g.s.} + {}^6\mathrm{He}_{g.s.})$ are shifted by 1.3 MeV to the lower energy side. As explained in Sec. III B, the 0^+_3 state with $\alpha + {}^8\mathrm{He}_{g.s.}$ appears around the respective decay threshold, and one-to-one correspondence between the levels and the thresholds is also clearly confirmed in other levels. The cluster structures with the chemical bonds of the neutrons change from level to level according to the threshold rules.

As shown in Fig. 6, all the threshold energies are confined within the range of $\sim$4 MeV, and the energy interval between neighboring thresholds is just $\sim$1 MeV. Because of the small spacings of the threshold energies, the mixing of the He-cluster components is strong, although the dominant component can be identified in each of the energy levels. In Table IV, the dominant populations calculated by $f^\gamma(S = 6\ \mathrm{fm})$ in Eq. (15) are shown. The squared amplitude of ${}^5\mathrm{He}_{g.s.} + {}^7\mathrm{He}_{g.s.}$ in 0^+_6 is the smallest of all the levels, and the dominant populations in the individual levels are about 50% on average. Thus, each level contains impurities besides a main component. Such a mixture of the impurities is important for reducing the decay width of the levels, as discussed in Refs. [28,35].

The level scheme of the unbound states nicely reproduces the features in the recent observation, obtained in the inelastic scattering of ${}^{12}\mathrm{Be}$ by an α target [24]. In this inelastic scattering, the 0^+ strength, which reveals the overlapping resonances with a distance of $\sim$ 1 MeV, is observed in the same energy region as the present calculation. Furthermore, there are at least two observed levels consistent to the calculated levels [29,35]; the calculated 0^+_3 and 0^+_5 states has a dominant decay width into the $\alpha + {}^8\mathrm{He}_{g.s.}$ and ${}^6\mathrm{He}_{g.s.} + {}^6\mathrm{He}_{g.s.}$

TABLE IV. The main component of the adiabatic states at $S = 6$ fm. The main populations represent $f^\gamma(S)$ shown in Eq. (15).

Levels	Main component (γ)	$f^\gamma(S = 6)$
0^+_3	$\alpha + {}^8\mathrm{He}_{g.s.}$	0.56
0^+_4	${}^6\mathrm{He}_{g.s.} + {}^6\mathrm{He}_{g.s.}$	0.63
0^+_5	$\tilde{\varphi}(L)\tilde{\varphi}(R)(\sigma^+_{1/2})^2$	0.61
0^+_6	${}^5\mathrm{He}_{g.s.} + {}^7\mathrm{He}_{g.s.}$ $(I = 2)$	0.28

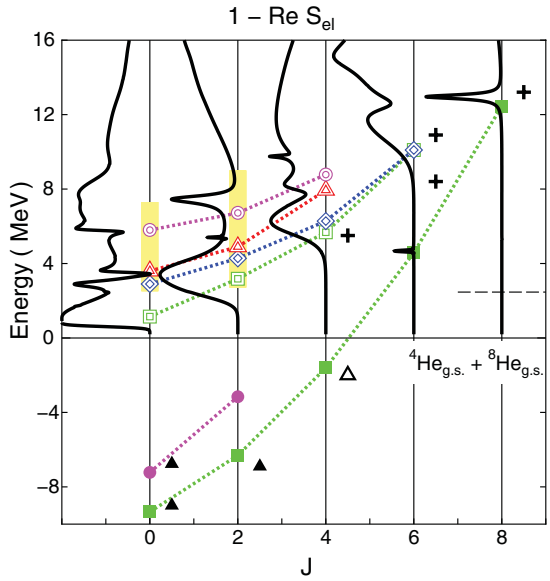

FIG. 7. (Color online) Rotational bands of ^{12}Be. The shaded area represents the region where the overlapping resonances are observed [24,25], while the solid triangles and the crosses show the data in Refs. [22] and [26], respectively. The spin assignment of the open triangle is tentative, and the data is taken from Ref. [27]. The resonance energies of Refs. [24–26] are measured from the calculated threshold of $^6\mathrm{He}_{g.s.} + {}^6\mathrm{He}_{g.s.}$. The dashed line at the right denotes the calculated threshold of $^6\mathrm{He}_{g.s.} + {}^6\mathrm{He}_{g.s.}$. See text for details.

channels, respectively, and the two levels having similar decay schemes are observed around the same energy regions. In a much deeper comparison of the theory with the experiments, the comparison of the partial decay width is important.

To compare the present calculation with the recent experiments over a wide energy and spin region, we perform a similar calculation for the nonzero spins. In the calculation for the nonzero spins, we restricted the AO basis with an axial symmetric configuration to identify the $K^\pi = 0^+$ bands clearly. Since the KHK method cannot be directly applied to the nonzero spin state in the restriction of $K^\pi = 0^+$, we employ the closed-state method [34–36]. In this method, we solve the coupling of the spinless open channels [$\alpha + {}^8\mathrm{He}_{g.s.}$, $^6\mathrm{He}_{g.s.} + {}^6\mathrm{He}_{g.s.}$, $^5\mathrm{He}_{g.s.} + {}^7\mathrm{He}_{g.s.}$ ($I = 0$)] and the intrinsic states obtained by diagonalizing the total Hamiltonian. The details of the closed-state method are explained in Ref. [36]. The rotational bands are shown in Fig. 7. In this figure, the partial reaction cross sections of the $\alpha + {}^8\mathrm{He}_{g.s.}$ scattering, which is defined by $1 - \Re S^J_{el}$ with the elastic S matrix S^J_{el} for spin J, are also plotted. We can clearly see the change of the bands from the bound states to the scattering states with the variation of the excitation energy.

The maximum spin of the ground rotational band (solid squares) reaches $J^\pi = 8^+$ because of the nature of the neutrons' $(\sigma^+_{1/2})^2$ configuration, which is the origin of the breaking of the $N = 8$ magic number [28]. The second band (solid circles) has the main component of a closed $0p$-shell configuration of the neutrons, and, hence, this band terminates at $J^\pi = 2^+$. Furthermore, four rotational bands appear in the continuum region. We can see the overlapping behavior of the $\alpha + {}^8\mathrm{He}_{g.s.}$ band (double squares) and the $^6\mathrm{He}_{g.s.} + {}^6\mathrm{He}_{g.s.}$ one (double diamonds) as the spin becomes high. This behavior occurs because coupling with the scattering continuum becomes strong in the high-spin region; hence, identifying these two bands as isolated states becomes difficult. In addition, the $^5\mathrm{He}_{g.s.} + {}^7\mathrm{He}_{g.s.}$ molecular band (double circles) appears with a moment of inertia comparable to those of the $\alpha + {}^8\mathrm{He}_{g.s.}$ and $^6\mathrm{He}_{g.s.} + {}^6\mathrm{He}_{g.s.}$ bands. The energy position of the SD band with covalent neutrons (double triangles) is quite close to the position of the molecular bands of the He dimer.

The present calculation nicely reproduces the energy-spin systematics of the experimental data observed as isolated levels from the bound region (solid triangles [22] and one open triangle [27]) to the continuum region (crosses [26]). In particular, the unbound states in the $J^\pi = 0^+$ and 2^+ states are located in the region of the shaded area where the many resonant structures are fragmented with overlapping features [24,25]. To obtain the resonances with small energy spacings, it is quite important to describe not only the internal MO states realized at the local minimum points in the AESs, but also the external He dimers appearing in the outside conjunction region. Our method covers the smooth connection of the internal MOs and the external He dimers, and, hence, such degenerate resonance phenomena can be reproduced.

C. Internal and external amplitudes in the energy levels

The final solutions in the energy levels shown in Figs. 5 and 6 contain both the components of the internal MO and the external He-dimer states identified in Table II. In this section, we investigate the population of the internal and external states in each energy level. Here we calculate the squared amplitude

$$h(\nu, \mu, S) = \left|\left\langle \Phi^\mu_{AS}(S)\middle|\Psi_\nu\right\rangle\right|^2, \tag{20}$$

where $\Phi^\mu_{AS}(S)$ represents the μth adiabatic states with $\mu = A \sim D$, shown in Fig. 2 and in Table II at the distance of S, while Ψ_ν is the full solution in Fig. 5 (0^+_ν, $\nu = 1 \sim 6$). From $h(\nu, \mu, S)$, we define the population of the internal (P_{in}) and external (P_{ex}) states, which are divided by a boundary of the conjunction distance, S_C, as in

$$P_{in}(\nu, \mu) = \int_{S_{\min}}^{S_C} dS h(\nu, \mu, S)/P_{\mathrm{tot}}(\nu, \mu), \tag{21}$$

$$P_{ex}(\nu, \mu) = \int_{S_C}^{S_{\max}} dS h(\nu, \mu, S)/P_{\mathrm{tot}}(\nu, \mu), \tag{22}$$

where $P_{\mathrm{tot}} = P_{in} + P_{ex}$. $P_{in}(\nu, \mu)$ [$P_{ex}(\nu, \mu)$] represents the population of the internal [external] state of the μth AES included in the νth energy level.

P_{in} and P_{ex} of the dominant adiabatic state in each level are shown in Table V. In this analysis, we set $S_{\min} = 2.0$ fm and $S_{\max} = 8.8$ fm. The upper two rows show the results for the low-lying bound states, while the results of the newly identified resonances are shown in the lower four rows. From this table, we can easily characterize the type of the

TABLE V. The squared amplitude of the internal and external states in the energy levels. The left-most column and the second one represent the number of the energy level (0_1^+–0_6^+) and the dominant AES, (A–D shown in Fig. 2 and Table II) for the respective energy level. In the third and fifth column from the left, the squared amplitude of the internal ($in.$) and the external ($ex.$) adiabatic states, which are divided by S_C (fourth column), are shown in units of %. The underlining represents the dominant population. In the second column from the right, the dominant configurations are shown.

ν	μ	P_{in}	S_C	P_{ex}	Main con.	Type
0_1^+	B	<u>96</u>	5.6	4	$(\pi_{3/2}^-)^2(\sigma_{1/2}^+)^2$	$in.$
0_2^+	A	<u>98</u>	4.8	2	$(\pi_{3/2}^-)^2(\pi_{1/2}^-)^2$	$in.$
0_3^+	B	22	5.6	<u>78</u>	$\alpha + {}^8\mathrm{He}$	$ex.$
0_4^+	C	<u>42</u>	5.6	<u>58</u>	${}^6\mathrm{He} + {}^6\mathrm{He}$	$in. + ex.$
0_5^+	D	<u>91</u>	7.2	9	$\tilde{\varphi}(L)\tilde{\varphi}(R)(\sigma_{1/2}^+)^2$	$in.$
0_6^+	A	24	4.8	<u>76</u>	${}^5\mathrm{He} + {}^7\mathrm{He}\ (I=2)$	$ex.$

energy levels in terms of either the internal state ($in.$) or the external state ($ex.$).

P_{in} for the bound states 0_1^+ and 0_2^+ exceeds 90%. Thus, a large part of the wave function is localized in the internal region, and its small fraction, $P_{ex.} \sim 5$ %, penetrates into the external region. The unbound 0_5^+ state can also be classified into the internal state, but its conjunction distance S_C is a 1.3–1.5 times larger value than that for the bound 0_1^+ and 0_2^+ states because of the hybrid structure of the ^{5}He dimer and the σ^+ orbital in the 0_5^+ state. Therefore, the 0_1^+, 0_2^+, and 0_5^+ states with $P_{in.} \sim 90$ % can be clearly classified into the internal state, although there is a difference among the conjunction distances.

In contrast to these internal states, the 0_3^+ and 0_6^+ states have a large P_{ex} of 80% and have a dominant configuration of the He dimer with a minor contribution of the internal state, $P_{in.} \sim 20\%$. This dominance of $P_{ex.}$ means that 0_3^+ and 0_6^+ can be characterized as the external states. In a similar classification, the 0_4^+ state has an intermediate character of the internal and external states because a strong mixture of both states with $P_{in.} \sim P_{ex.} \sim 50\%$ occurs in this state. By introducing the conjunction distance S_C, the intrinsic structure can be characterized in terms of the internal and external states as well as its dominant configuration, which is often used in the structural analysis.

D. Classification of the excited energy levels

We summarize the identified energy levels as follows: The internal MO states, $(\pi_{3/2}^-)^2(\sigma_{1/2}^+)^2$ in 0_1^+ and $(\pi_{3/2}^-)^2(\pi_{1/2}^-)^2$ in 0_2^+, appear in the bound region. These two states are obtained by the rearrangements of the pair of neutrons, $(\sigma_{1/2}^+)^2 \leftrightarrow (\pi_{1/2}^-)^2$. In addition to bound MO states, we newly identified the four resonant states, and the internal and external states coexist in the resonant states. The He dimers, such as $\alpha + {}^8\mathrm{He}_{g.s.}$ in 0_3^+ and ${}^5\mathrm{He}_{g.s.} + {}^7\mathrm{He}_{g.s.}$ in 0_6^+, are the external state, while ${}^6\mathrm{He}_{g.s.} + {}^6\mathrm{He}_{g.s.}$ in 0_4^+ and $\tilde{\varphi}(L)\tilde{\varphi}(R)(\sigma_{1/2}^+)^2$ in 0_5^+ are classified into the intermediate state (internal + external) and the extended internal states, respectively. All of these

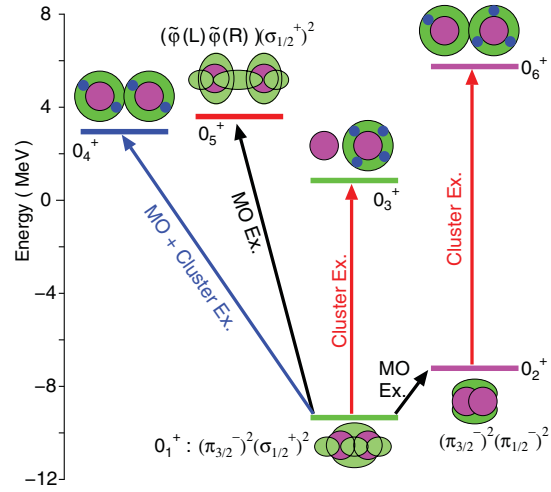

FIG. 8. (Color online) Energy spectra classified by the excitation degrees of freedom ($J^\pi = 0^+$). See text for details.

resonances are confined inside of the α-α Coulomb barrier with a mean height of about 1.5 MeV.

According to the classification of the internal and external states, we identify the excitation degrees of freedom for individual excited levels. The excitation schemes are shown in Fig. 8 and are summarized as follows:

(1) Molecular orbital (MO) excitation. The 0_2^+ and 0_5^+ states have a large population of internal MO states because they correspond to the local minimum states in AESs (A) and (D), respectively. The ground state is also an internal MO state generated by the AES (B) and, hence, the 0_2^+ and 0_5^+ states can be characterized by the molecular orbital excitation of the neutrons from the ground 0_1^+ state. These excitations involve the pair rearrangements of the neutrons: $(\sigma_{1/2}^+)^2 \rightarrow (\pi_{1/2}^-)^2$ for 0_2^+ and $(\pi_{3/2}^-)^2 \rightarrow \tilde{\varphi}(L)\tilde{\varphi}(R)$ for 0_5^+. The MO excitations are not a static excitation of the neutrons around a spatially fixed two α particle, but a dynamic excitation which strongly couples to the breathing of the two α cores.

(2) Cluster excitation. The 0_3^+ state has a dominant amplitude of the external state of the AES (B), which has the main component of $\alpha + {}^8\mathrm{He}_{g.s.}$. Specifically, the formation of 0_3^+ involves the extension of the α-α distance, and the 0_3^+ state is formed by the nodal excitation of the α-α relative wave function from the 0_1^+ state, which is the internal state of the AES (B). In a similar classification, the 0_6^+ state with ${}^5\mathrm{He}_{g.s.} + {}^7\mathrm{He}_{g.s.}$ corresponds to the excited state of the two-α relative motion from the 0_2^+ state. The 0_3^+ and 0_6^+ states are the higher nodal states in the α-α relative wave function from the 0_1^+ and 0_2^+ states, respectively.

(3) Double excitation. The main component of 0_4^+ is the AES (C), and the state contains both the internal and external states. The coexistence of two regions is a strong mixture of the internal MO state of $(\pi_{3/2}^-)^2(\pi_{3/2}^+)^2$ and the external ${}^6\mathrm{He}_{g.s.} + {}^6\mathrm{He}_{g.s.}$ state. Therefore, the 0_4^+ state is generated by the double excitation of both the α-α relative motion and the molecular orbits of the neutrons.

In $^{12}\mathrm{Be} = \alpha + \alpha + 4N$, two degrees of freedom exist: the α-α relative motion and the single-particle motion of the four

excess neutrons. All the excited states are realized as a result of the excitation of these two degrees of freedom. Recent studies have shown that the excitation of the cluster degrees of freedom involves the enhancement of the monopole transition [42]. The detailed analysis of the monopole transition in ^{12}Be is shown in Ref. [29]. According to the result, all the monopole strengths of $0_1^+ \rightarrow 0_{ex.}^+$ are comparable to or larger than the single-particle strength [29], and a transition from the ground 0_1^+ state to its higher nodal state, 0_3^+, is especially enhanced.

V. SUMMARY AND DISCUSSION

In sum, the generalized two-center cluster model (GTCM), which can handle covalent and atomic configurations in general two center systems, is applied to the light neutron-excess system, $^{12}\mathrm{Be} = \alpha + \alpha + 4N$. The changes of the orbits of the neutrons are analyzed by calculating adiabatic energy surfaces with a variation of the α-α distance. We pursue a smooth transition from the covalent molecular orbits (MOs) to the atomic He-dimer states, which are realized in the adiabatic energy surfaces. The covalent MO structures are realized at the local minimum points in the inner AESs, while the He dimers appear at the asymptotic region of the α-α distance. According to the smooth transition, the adiabatic states are divided into two regions, the internal MO region and the external He-dimer region, by introducing boundaries of the conjunction distance S_C.

In the calculation of the energy levels, four resonant states are newly discovered above the α-decay threshold in addition to the two bound MO states, which have already been studied in previous works [13,28]. One-to-one correspondence between all four resonant levels and the respective thresholds is observed. Specifically, the various chemical-bonding-like states appear according to the threshold rule. The newly obtained resonances reproduce nicely the observed energy-spin systematics; hence, the present treatment based on the $\alpha + \alpha + 4N$ model can describe the global features of ^{12}Be. This result strongly supports the claim that ^{12}Be should be considered a system that potentially has this six-particle degree of freedom, and a similar picture is expected to be valid for the heavier isotope, $^{14}\mathrm{Be} = \alpha + \alpha + 6N$.

By introducing the identified conjunction distance S_C, which is a boundary of the internal and external states, it is possible to characterize the energy levels with three MO structures and three He-dimer structures in terms of either the internal states inside of S_C or the external states outside of S_C. Two bound states are almost pure internal states, in which the squared amplitude of the internal region, P_{in}, exceeds about 90%. In contrast, a large mixture of the external state occurs, and the population of P_{ex} reaches about 80% in the 0_3^+ state with the $\alpha + {}^8\mathrm{He}_{g.s.}$ structure, for instance. Because of the orthogonality to two internal MO states, the internal amplitude P_{in} is suppressed in the four resonant states, and a large mixture of P_{ex} strongly occurs. According to the classification using S_C, all the energy levels are characterized by the excitation degrees of freedom: either the α-α relative excitation or the molecular orbital excitation of the four neutrons. The former excitation represents the nodal excitation

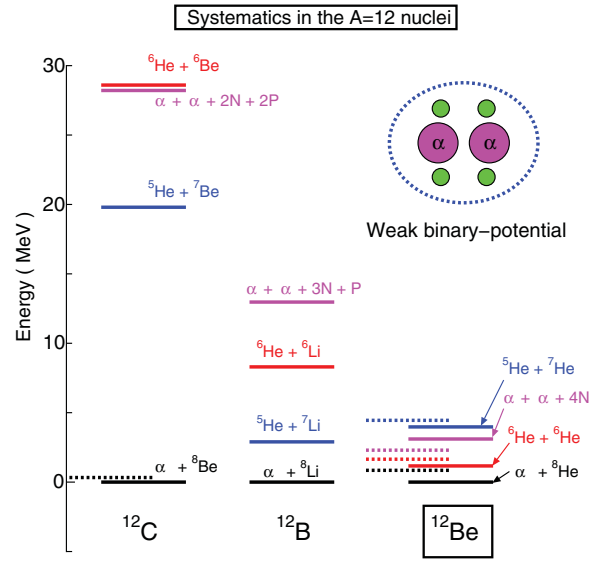

FIG. 9. (Color online) Threshold and level scheme of ^{12}C, ^{12}B, and ^{12}Be. The threshold energies of the α emission are taken to be the origins. The energy levels are plotted by the dotted lines, while the threshold energies are shown by the solid lines. The threshold energy for the decay into two α plus four nucleons is also plotted.

of the α-α relative wave function, while the rearrangements of the MO orbits of the neutrons occur in the latter excitation. In particular, the direct α-α excitation from the ground state can be observed as the enhancement phenomena in the monopole transition.

The energy intervals of the resonant levels are quite small, and the levels have a strong degeneracy. This degeneracy is peculiar to the neutron-excess system, ^{12}Be, and we can easily understand its peculiarity in the $A = 12$ systematics illustrated in Fig. 9. In this figure, the α decay threshold energies are set to be a zero-energy point, and various thresholds obtained by the neutron's or proton's rearrangements from the lowest α threshold are plotted by the solid lines. The six-body-breakup threshold of $\alpha + \alpha +$ nucleons (N = neutron and P = proton) are also plotted for the individual nuclei.

In ^{12}Be, the threshold energies are located with a mean interval of less than 1 MeV, but the interval of the thresholds becomes large in ^{12}B (∼4 MeV). In ^{12}C with $N = Z$, there are large energy intervals in the threshold energies, which are about 7 MeV on average. This interval is larger by about one order of magnitude than that of ^{12}Be, and the thresholds in ^{12}Be reveal a strong degenerate feature in a comparison with those in ^{12}C. This difference between ^{12}C and ^{12}Be is attributed to a change of the building blocks in the system. The ^{12}C nucleus is described nicely by the 3α particle, while, in ^{12}Be, four excess neutrons are weakly coupled to two α cores. Since a large amount of energy is needed to break an α particle in $^8\mathrm{Be}_{g.s.} = \alpha + \alpha$, the threshold interval in ^{12}C is much larger than that in ^{12}Be.

The Hoyle state identified around the $\alpha + {}^8\mathrm{Be}_{g.s.}$ threshold has an almost pure $\alpha + {}^8\mathrm{Be}_{g.s.}$ structure [2] because there are no other thresholds with the rearrangements of the neutrons near the Hoyle state. In contrast to the $N = Z$ system, the levels in ^{12}Be contain a considerable amount of impurities

due to the threshold degeneracy and hence, they are not rigid clusters by comparison to the normal α-cluster states in $N = Z$ systems. In this situation, the unbound He dimers in ^{12}Be should be called "loose clusters." The loose clusters mean that the $^{4-8}$He nuclei form a main cluster component corresponding to the He-decay threshold, but the constituent two-He clusters can easily emit and/or absorb the neutrons due to a small threshold difference. The rearrangements of the neutrons easily occur because the binary potentials are weak, such as α-N, neutron-neutron, and α-α, in which no bound states exist. The weakness of the interaction between clusters and excess neutrons is a common feature in neutron-excess systems. Therefore, the results of the present study strongly suggest that the loose clusters can be observed in a wide range of systems close to the drip line of the neutrons. Systematic studies are now under way in light nuclear systems.

ACKNOWLEDGMENTS

The author would like to thank Professor K. Ikeda for carefully reading this manuscript and making useful comments. The author also thanks Professors H. Horiuchi, T. Nakatsukasa, H. Sakurai, K. Katō, N. Itagaki, S. Shimoura, and Dr. A. Saito for useful discussions and encouragement. This work has been supported by a Grant-in-Aid for scientific Research in Japan (No. 18740129 and No. 21740211). The author also would like to thank the JSPS core-to-core program. The numerical calculation was performed at RSCC, RIKEN.

[1] K. Ikeda *et al*., Prog. Theor. Phys. **68**, 1 (1980), and references therein.
[2] Y. Fukushima and M. Kamimura, in *Proceedings of the International Conference on Nuclear Structure*, J. Phys. Soc. Jpn. Suppl. **44**, 225 (1978); M. Kamimura, Nucl. Phys. A **351**, 456 (1981).
[3] E. Uegaki, S. Okabe, Y. Abe, and M. Tanaka, Prog. Theor. Phys. **57**, 1262 (1977); **62**, 1621 (1979).
[4] Y. Suzuki, Prog. Theor. Phys. **55**, 1751 (1976); **56**, 111 (1976).
[5] T. Matsuse, M. Kamimura, and Y. Fukushima, Prog. Theor. Phys. **53**, 706 (1975).
[6] A. Tohsaki, H. Horiuchi, P. Schuck, and G. Röpke, Phys. Rev. Lett. **87**, 192501 (2001); Y. Funaki, A. Tohsaki, H. Horiuchi, P. Schuck, and G. Röpke, Phys. Rev. C **67**, 051306(R) (2003), and references therein.
[7] M. Ito, Y. Hirabayashi, and Y. Sakuragi, Phys. Rev. C **66**, 034307 (2002); M. Ito, Y. Sakuragi, and Y. Hirabayashi, *ibid*. **63**, 064303 (2001); Eur. Phys. J. A **5**, 373 (1999).
[8] K. Ikeda, N. Takigawa, and H. Horiuchi, Prog. Theor. Phys. Suppl. Extra Number (1968), 464 .
[9] K. Wildermuth and Y. C. Tang, Phys. Rev. Lett. **6**, 17 (1961).
[10] D. M. Brink, J. Phys.: Conf. Ser. **111**, 012001 (2008).
[11] Y. Abe, J. Hiura, and H. Tanaka, Prog. Theor. Phys. **49**, 800 (1973).
[12] N. Itagaki and S. Okabe, Phys. Rev. C **61**, 044306 (2000), and references therein.
[13] N. Itagaki, S. Okabe, and K. Ikeda, Phys. Rev. C **62**, 034301 (2000), and references therein.
[14] H. Furutani *et al*., Suppl. Prog. Theor. Phys. **68**, 193 (1980); M. Seya, M. Kohno, and S. Nagata, Prog. Theor. Phys. **65**, 204 (1981).
[15] N. Itagaki, S. Okabe, K. Ikeda, and I. Tanihata, Phys. Rev. C **64**, 014301 (2001); N. Itagaki, W. von Oertzen, and S. Okabe, *ibid*. **74**, 067304 (2006).
[16] Y. Kanada-En'yo and H. Horiuchi, Phys. Rev. C **68**, 014319 (2003).
[17] W. von Oertzen, Z. Phys. A **354**, 37 (1996).
[18] W. von Oertzen, Z. Phys. A **357**, 355 (1997).
[19] W. von Oertzen, Eur. Phys. J. A **11**, 403 (2001).
[20] Masaaki Kimura, Phys. Rev. C **75**, 034312 (2007).
[21] H. Iwasaki *et al*., Phys. Lett. B **481**, 7 (2000); **491**, 8 (2000).
[22] S. Shimoura *et al*., Phys. Lett. B **560**, 31 (2003); **654**, 87 (2007).
[23] A. A. Korsheninnikov *et al*., Phys. Lett. B **343**, 53 (1995).
[24] A. Saito *et al*., Suppl. Prog. Theor. Phys. **146**, 615 (2003); A. Saito, Ph.D. thesis, Rikkyo University, 2006 (unpublished). A. Saito *et al*., AIP Conf. Proc. **891**, 205 (2006).
[25] A. Saito *et al*., Mod. Phys. Lett. A **25**, 1858 (2010).
[26] M. Freer *et al*., Phys. Rev. Lett. **82**, 1383 (1999); Phys. Rev. C **63**, 034301 (2001).
[27] H. G. Bohlen *et al*., J. Phys.: Conf. Ser. **111**, 012021 (2008).
[28] M. Ito, N. Itagaki, and K. Ikeda, Phys. Rev. C **85**, 014302 (2012).
[29] M. Ito, Phys. Rev. C **83**, 044319 (2011).
[30] P. Descouvemont and D. Baye, Few-Body Syst. **29**, 131 (2000); Phys. Lett. B **505**, 71 (2001).
[31] M. Ito and Y. Sakuragi, Phys. Rev. C **62**, 064310 (2000).
[32] M. Ito, K. Kato and K. Ikeda, Mod. Phys. Lett. A **18**, 178 (2003); Phys. Lett. B **588**, 43 (2004).
[33] M. Ito, Phys. Lett. B **636**, 293 (2006); Mod. Phys. Lett. A **21**, 2429 (2006).
[34] M. Ito, N. Itagaki, H. Sakurai, and K. Ikeda, Phys. Rev. Lett. **100**, 182502 (2008); J. Phys.: Conf. Ser. **111**, 012010 (2008); RIKEN RESEARCH **3**, No. 9 (2008) [http://www.rikenresearch.riken.jp/eng/research/5456].
[35] M. Ito and N. Itagaki, Phys. Rev. C **78**, 011602(R) (2008); Phys. Rev. Focus **22**, 4 (2008).
[36] M. Ito and D. Suzuki, Phys. Rev. C **84**, 014608 (2011).
[37] H. Horiuchi *et al*., Suppl. Prog. Theor. Phys. **62**, 90 (1977).
[38] M. Ito, K. Yabana, T. Nakatsukasa, and M. Ueda, Phys. Lett. B **637**, 53 (2006).
[39] K. Ikeda *et al*., Prog. Theor. Phys. Suppl. **52**, 33 (1972).
[40] M. Ito and K. Yabana, Prog. Theor. Phys. **113**, 1047 (2005).
[41] M. Kamimura, Prog. Theor. Phys. Suppl. **62**, 236 (1977).
[42] T. Yamada, Y. Funaki, H. Horiuchi, K. Ikeda, Y. Funaki, and A. Thosaki, Prog. Theor. Phys. **120**, 1139 (2008).